CrossMark

# Intermediate-mass Stars Become Magnetic White Dwarfs

Ilaria Caiazzo[1,2,8] , Jeremy Heyl[2] , Harvey Richer[2] , Jeffrey Cummings[3,4] , Leesa Fleury[2] , James Hegarty[2] ,
Jason Kalirai[5], Ronan Kerr[6], Sarah Thiele[2], Pier-Emmanuel Tremblay[7] , and Michael Villanueva[2]

[1] Walter Burke Institute for Theoretical Physics, TAPIR, Caltech, Mail Code 350-17, Pasadena, CA 91125, USA; ilariac@caltech.edu
[2] University of British Columbia, Department of Physics and Astronomy, Vancouver BC V6T 1Z1, Canada
[3] Space Telescope Science Institute, 3700 San Martin Drive, Baltimore, MD 21218, USA
[4] Johns Hopkins University, Department of Physics and Astronomy, 3400 North Charles Street, Baltimore, MD 21218, USA
[5] Applied Physics Laboratories, Johns Hopkins University, Baltimore, MD 21218, USA
[6] University of Texas at Austin, Department of Astronomy, Austin, TX 78712-1205, USA
[7] University of Warwick, Department of Physics, Coventry CV4 7AL, UK
Received 2020 July 28; revised 2020 September 4; accepted 2020 September 6; published 2020 September 22

## Abstract

When a star exhausts its nuclear fuel, it either explodes as a supernova or more quiescently becomes a white dwarf, an object about half the mass of our Sun with a radius of about that of the Earth. About one-fifth of white dwarfs exhibit the presence of magnetic fields, whose origin has long been debated as either the product of previous stages of evolution or of binary interactions. We here report the discovery of two massive and magnetic white-dwarf members of young star clusters in the Gaia second data release (DR2) database, while a third massive and magnetic cluster white dwarf was already reported in a previous paper. These stars are most likely the product of single-star evolution and therefore challenge the merger scenario as the only way to produce magnetic white dwarfs. The progenitor masses of these stars are all above 5 solar masses, and there are only two other cluster white dwarfs whose distances have been unambiguously measured with Gaia and whose progenitors' masses fall in this range. This high incidence of magnetic white dwarfs indicates that intermediate-mass progenitors are more likely to produce magnetic remnants and that a fraction of magnetic white dwarfs forms from intermediate-mass stars.

## 1. Introduction

White dwarfs (WDs) are all born in the same manner, as the compact remnants of low- and intermediate-mass stars up to about eight times the mass of our Sun. However, some WDs are peculiar, as their surfaces are threaded with magnetic fields that range from a few thousand to a billion Gauss. A recent study (Landstreet & Bagnulo 2019) that focused on DA (hydrogen atmosphere) WDs showed that about $20 \pm 5\%$ of the 80 DA WDs that are within 20 pc of the Sun are magnetic, of which only seven ($\sim$9%) have magnetic fields exceeding 1 MG. If we extend the sample to all the WDs within 20 pc of the Sun (Hollands et al. 2018), we find a similar result: of the 126 WDs that have a spectral classification, about 20% (23) are magnetic and about 10% (13) have magnetic fields above 0.5 MG. The origin of magnetism in WDs is still a matter of debate, and the theories that have been suggested fall into two main categories. In one model, the binary scenario, magnetic fields in WDs are created by the convective dynamos that arise during a common envelope phase in the interaction with a companion star (Tout et al. 2008; Nordhaus et al. 2011; García-Berro et al. 2012; Wickramasinghe et al. 2014). In this case, a magnetic WD would either be the product of a merger or would still be in a close binary. In the main alternative hypothesis, the magnetic fields found in WDs are thought to be of fossil origin; that is, they were already present in the progenitor star or somehow were generated in the different evolutionary stages that precede the formation of the WD. In this second scenario, the progenitors could be stars that already displayed strong

magnetic fields, such as the magnetic main-sequence Ap/Bp stars (Woltjer 1964; Moss 2003; Tout et al. 2004), or the magnetic field could be hidden in the progenitor stars' core, as is suggested by recent studies on asteroseismology of red giant stars (Fuller et al. 2015; Cantiello et al. 2016; Stello et al. 2016).

It is well known that magnetic WDs are on average more massive than non-magnetic ones (Ferrario et al. 2020; Kawka 2020; McCleery et al. 2020), and this could either indicate that the mass of the progenitor star is somehow related to the genesis of the magnetic field, as more massive stars create more massive WDs, or that magnetic WDs are the products of WD mergers, or both. We here report the discovery of two DA WDs from the Gaia second data release (DR2) catalog (Gaia Collaboration et al. 2016, 2018) in young open star clusters that exhibit the presence of a magnetic field on their surface. The WDs are located in Messier 39 (M 39, NGC 7092) and ASCC 47. We already reported the discovery of a third magnetic DB (helium atmosphere) WD in Messier 47 (M 47) in Richer et al. (2019, hereafter Paper I). ASCC 47 is the youngest open cluster ($90 \pm 20$ Myr) known to contain a WD, and the WD itself is the youngest and hottest found in such a cluster; M 39 is $280 \pm 20$ Myr old and M 47 is $150 \pm 20$ Myr old (see below). As such young clusters could have only produced massive WDs above $\sim$0.9 $M_\odot$ (Cummings et al. 2018), a merger inside the cluster would have created a remnant that is above the maximum mass for a WD (the Chandrasekhar limit of 1.38 $M_\odot$; Nomoto 1987), and therefore would have exploded in a type Ia supernova (Shen 2015). Furthermore, the fraction of binaries among the most massive stars in the cluster is low. For these reasons, the newly

discovered WDs rule out the double-degenerate merger scenario as the only channel for the formation of magnetic white dwarfs.

The fact that the three WDs are members of star clusters means that the mass of their progenitor stars can be inferred from the age of the cluster and from the cooling time of the WD. We find that the progenitor stars of the three WDs all had masses above 5 $M_\odot$, and there are only two other cluster WDs known in the Gaia DR2 database whose progenitors were this massive. This high incidence of magnetic WDs from intermediate-mass progenitors suggests that more massive stars are more likely to produce magnetic WDs, which would also explain why magnetic WDs are on average more massive.

## 2. Identification of the Objects

The publication of more than a billion high-precision parallaxes and proper motions in Gaia DR2 (Gaia Collaboration et al. 2016, 2018) has been revolutionary for many branches of stellar astrophysics. In the case of nearby open clusters, which can extend up to several square degrees on the sky, the identification of cluster members via the measurement of parallaxes and proper motions over large parts of the sky was not feasible previously for many clusters but has become straightforward with Gaia. The three WDs analyzed in this Letter were discovered as part of a larger survey of young open clusters whose purpose is to find massive cluster white dwarfs (H. Richer et al. 2020, in preparation). The WDs are identified as cluster members with high confidence because they lie inside cluster boundaries in coordinate space and have parallaxes and proper motions similar to those of their respective clusters, as can be seen in Figure 1 (for more details on each object, see Appendix A and Paper I).

To confirm the white-dwarf nature of the candidates, and to provide an estimate of their temperatures and surface gravities, we obtained their spectra with GMOS in long-slit mode on Gemini North (for the WD in M 39) and Gemini South (for the WD in ASCC 47), exploiting its fast turnaround program. The spectrum for the WD in M 47 was already obtained and published in Paper I. We used the B600 grating centered at 512 and 508 nm (for dithering) with no blocking filter. The slit width, set to 1″, provided about 5 Å resolution. We used IRAF (Tody 1986) for reduction.

## 3. Properties of the White Dwarfs

### 3.1. Magnetic Field

The spectra for the objects in ASCC 47 and M 39 are consistent with hot, massive DA WDs: the only spectral features are the hydrogen Balmer lines, which are very broad. In Figure 2 the lines have been plotted using equal ranges on the $x$ and $y$-axis, so it is possible to compare the two WDs; the lines for the ASCC 47 WD are extremely weak because the object is very hot. In the lower panels of Figure 2 we can see the H$\alpha$ lines for both objects, which show Zeeman splitting. For magnetic fields lower than about 10 MG, the effect of the magnetic field reduces to the linear Zeeman effect, for which the Balmer lines split into three components, with a central component at the same wavelength as the zero-field line and with a blueshifted and a redshifted component. The separation between the H$\alpha$ Zeeman components in both objects is about 20 Å, which corresponds to a field of about 1 MG. For the WD in M 47, the Zeeman splitting of the helium absorption lines indicates a magnetic field strength of 2.5 MG (see Paper I). As the observed Zeeman splitting represents the mean field across the surface of the star, the value of the polar magnetic field is bound to be higher.

### 3.2. Temperature, Surface Gravity, and Mass

The left panels of Figure 2 show the fit of non-magnetic atmosphere models to four Balmer lines: H$\beta$, H$\gamma$, H$\delta$, and H$\epsilon$. The fitting routine is explained in Appendix B and returns the following best-fitting values for the logarithm of the surface gravity ($\log g$) and for the effective temperature ($T_{\rm eff}$): $\log g = 8.87 \pm 0.07$ [log(cm s$^{-2}$)] and $T_{\rm eff} = 18,400 \pm 300$ K for the WD in M 39, and $\log g = 8.99 \pm 0.13$ [log(cm s$^{-2}$)] and $T_{\rm eff} = 116,000 \pm 3000$ K for ASCC 47. For both stars, the non-magnetic fit returns a surface gravity that is too high if we take into account the brightness of the WDs. In Figure 3, we plot the observed absolute magnitudes for the WDs (small points with error bars) and the magnitudes expected for WDs with the temperatures and surface gravities obtained from spectroscopy (hexagons with error bars). The discrepancy lies in the expected radii for the given surface gravities: comparing synthetic photometric models (Bergeron et al. 2001; Holberg & Bergeron 2006; Kowalski & Saumon 2006; Tremblay et al. 2011; Blouin et al. 2018) to the photometry available in Gaia, VPHAS+ (Drew et al. 2014), and Pan-STARRS (Chambers et al. 2016), we measure the WD radii to be 6100 ± 150 km for M 39 and 6750 ± 250 km for ASCC 47. Using the $\log g$ that we found from spectroscopy, these radii would imply an unreasonable mass of 2.1 $M_\odot$ for M 39 and 3.4 $M_\odot$ for ASCC 47, well above the Chandrasekhar limit of 1.38 $M_\odot$ (Nomoto 1987). This discrepancy is due to the magnetic field: the effect of surface gravity and magnetic field are degenerate in broadening the lines.

Because of this degeneracy, we cannot measure the surface gravity from spectroscopy and therefore we use photometric fitting (as in Gentile Fusillo et al. 2019, see Appendix C). We obtain the following values: $\log g = 8.54 \pm 0.04$ [log(cm s$^{-2}$)] for M 39, and $\log g = 8.47 \pm 0.05$ [log(cm s$^{-2}$)] for ASCC 47, which yield a mass of $0.95 \pm 0.02$ $M_\odot$ for M 39 and $1.01 \pm 0.02$ $M_\odot$ for ASCC 47. The photometric fit for the WD in M 47 returns a mass of $1.06 \pm 0.05$ $M_\odot$.

The right panels of Figure 2 show fits with simple magnetized atmospheric models that include the linear Zeeman effect assuming the field to be constant over the surface (see Appendix B). Since the effects of surface gravity and magnetic field are somewhat degenerate in broadening the lines, we kept the surface gravity fixed to the value obtained from photometry, and fitted for the best values of the magnetic field and temperature. We find that models with a magnetic field of 1.4 MG for M 39 and of 1.6 MG for ASCC 47 are an equally good fit to the Balmer lines as the non-magnetic models with the much higher surface gravities mentioned above. For both WDs, the magnetized fits result in slightly lower effective temperatures: 18,000 ± 340 K for M 39 and 110,000 ± 4000 K for ASCC 47. The magnetized atmosphere models are quite simplistic, but the fit shows that the excessive broadening can be explained by the presence of the magnetic field and returns magnetic field values that are comparable with what we can infer from the Zeeman splitting of H$\alpha$.
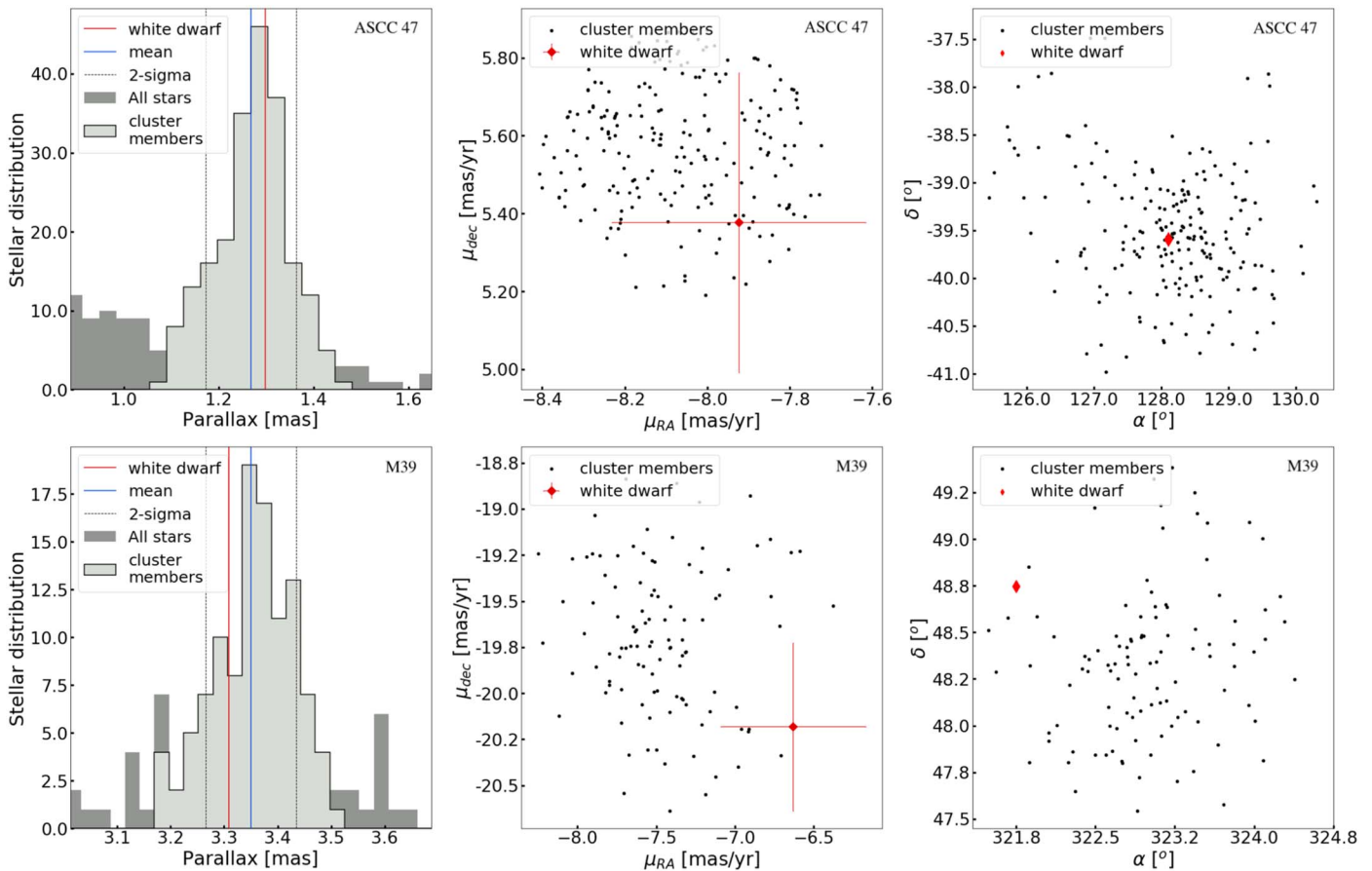
**Figure 1.** Phase-space cuts to determine the cluster membership: parallax, proper motion, and position on the sky. In the left panels, the gray histogram shows the distribution of parallaxes centered on the directions of ASCC 47 and M 39 within 2°.5 and 1°.5 of the centers of the two clusters. The blue line indicates the mean cluster values (1.273 and 3.350 mas), while the dashed lines delineate the $\pm 2\sigma$ parallax limits. The solid red line provides the measured parallax of the WD. The middle panels show the proper motions of the stars with the WD in red. The right panel shows the sky positions of the stars and the WD (again in red).

## 4. Initial–Final Mass Relation

By measuring the age of the cluster and the cooling age of the WDs, we can estimate the mass of the progenitor star. We fit isochrones generated with the PARSEC (Bressan et al. 2012) and MIST models (Paxton et al. 2011, 2013, 2015; Choi et al. 2016; Dotter 2016) to estimate the age of each of the clusters (the results for ASCC are depicted in Figure 4), which is also the total age of the WD including its lifetime before becoming a WD. We use the techniques developed in Cummings & Kalirai (2018). The age of the cluster ASCC 47 is 90 ± 20 Myr and that of M 39 is 280 ± 20 Myr. We estimated the age of M 47 to be 150 ± 20 Myr in Paper I. Both clusters are old enough that the age determination is not affected by stellar rotation (Cummings & Kalirai 2018). We subtract the age of the WD determined from the white-dwarf cooling models (Bergeron et al. 2001) from the cluster ages to determine the lifetime of the star that became the white dwarf and therefore its initial mass.

By measuring the cooling ages of the three WDs, we find that they all have progenitors with zero-age-main-sequence masses above 5 $M_\odot$ (see the values in Table 1). Among the WDs found in the Gaia catalog to be unequivocally members of clusters, there are only two other objects with progenitor masses above 5 $M_\odot$: EGGR 25 (LB 1497) and GD 50 (Dobbie et al. 2006), both in blue in Figure 5 (for more details see Appendix D). We re-analyzed the spectra of these two objects

using available spectroscopic data (Gianninas et al. 2011) and we do not find any indication of a magnetic field. Therefore, among known cluster WDs with progenitor masses above 5 $M_\odot$, we find that three out of five are magnetic, a higher percentage than the 15%–25% found in general (Kawka & Vennes 2004; Kawka et al. 2007; Landstreet & Bagnulo 2019) or of the ~10% found with magnetic fields exceeding 0.5 MG (Hollands et al. 2018; Landstreet & Bagnulo 2019). If the underlying fraction of magnetic white dwarfs in the clusters was similar to that within 20 pc (i.e., about 20%), one would find three or more magnetic white dwarfs out of a sample of five only 5.8% of the time. On the other hand, if we focus only on nearby white dwarfs with fields stronger than 1 MG (as we found in the clusters), the local fraction is even smaller (seven out of 123); in this case, even allowing for uncertainties in the local frequency of white dwarfs with fields greater than 1 MG, the chance of finding three or more magnetic white dwarfs out of five would be less than 0.5%. Therefore, we can reject the hypothesis that the intermediate-mass progenitor white dwarfs examined in this Letter have a similar fraction of stars with fields greater than 1 MG as the local sample at the 2-$\sigma$ or 3-$\sigma$ level. To find the confidence intervals on the frequency of magnetic WDs in open clusters we use a binomial distribution (which is appropriate for this situation), and a flat prior on the frequency because ours is the first measurement. We find the fraction of magnetic white dwarfs produced from intermediate-
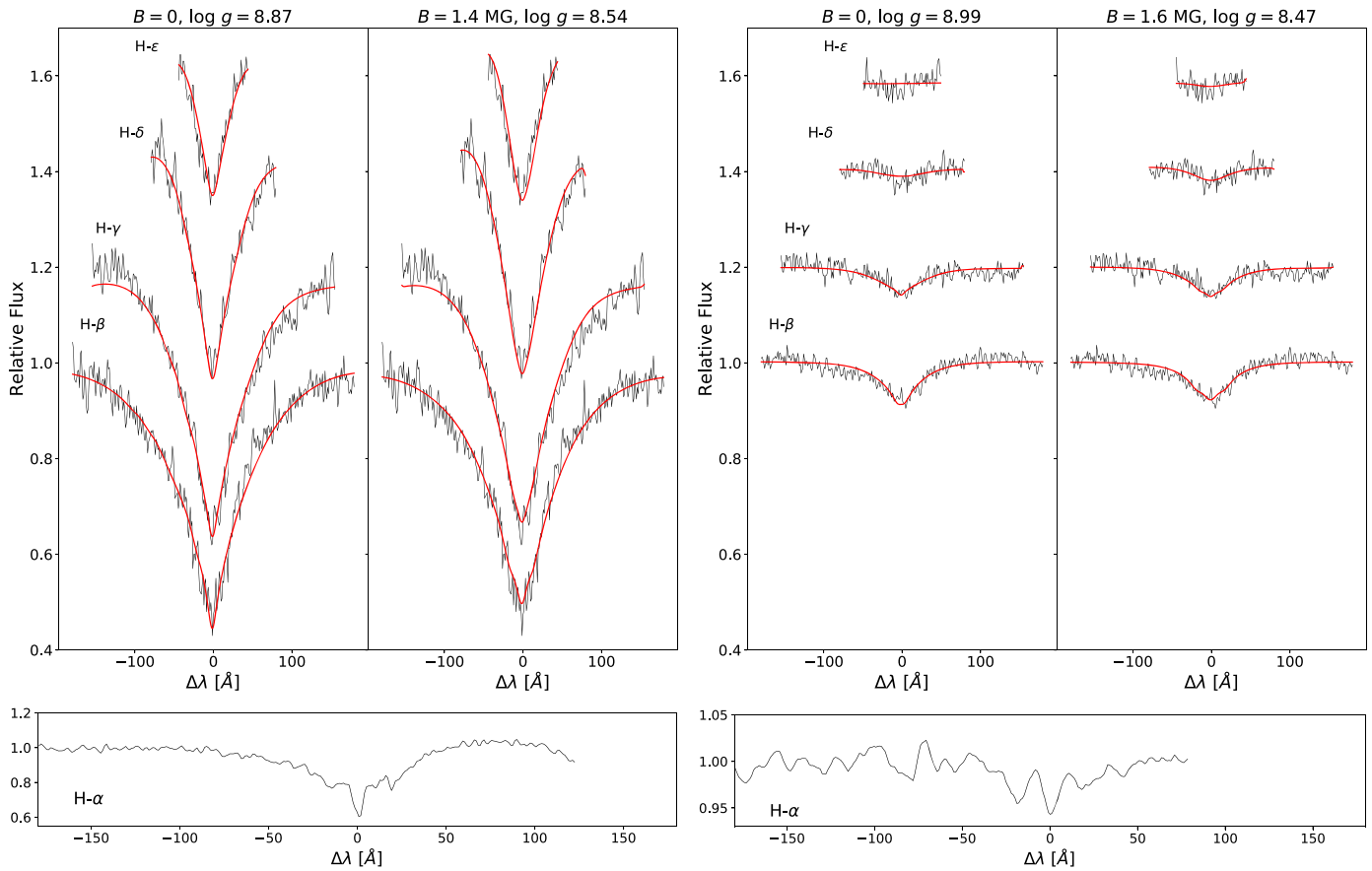
**Figure 2.** Top row: Balmer lines (Hβ to Hε) in the normalized spectra of M 39 (left) and ASCC 47 (right). Higher-order lines than Hβ have been shifted up by 0.2 each. In each panel, in red, the left side shows the best fit with the non-magnetic models and the right side with magnetic models. The values for the best fits are given in the text. Bottom row: Hα in M 39 (left) and ASCC 47 (right).
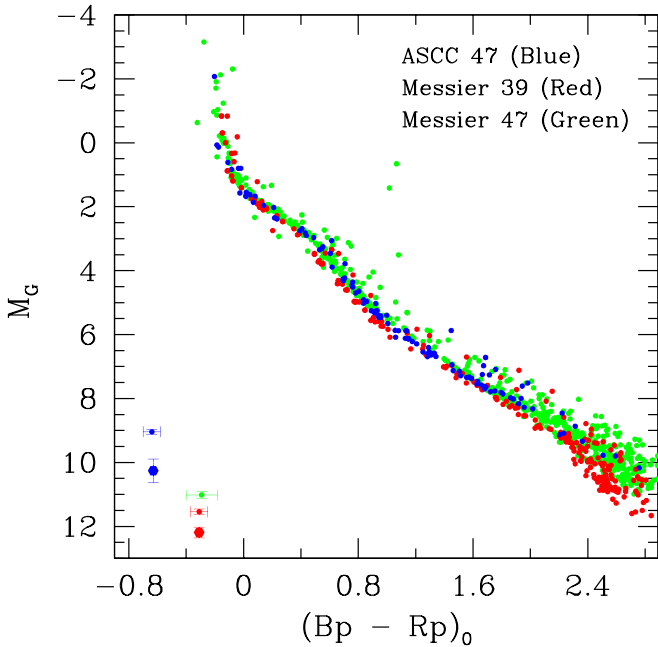


**Figure 3.** Gaia color–magnitude diagram (CMD) for the three clusters. The WDs can be seen in the lower-left corner. The observed values are indicated as small dots with error bars (from Gaia). For M 39 and ASCC 47, the hexagonal shape indicates the expected location in the CMD of the WDs for the log$g$ and $T_{eff}$ found from spectroscopy using the models by Tremblay et al. (Tremblay et al. 2011; the error bars come from 1-σ errors in the fit).
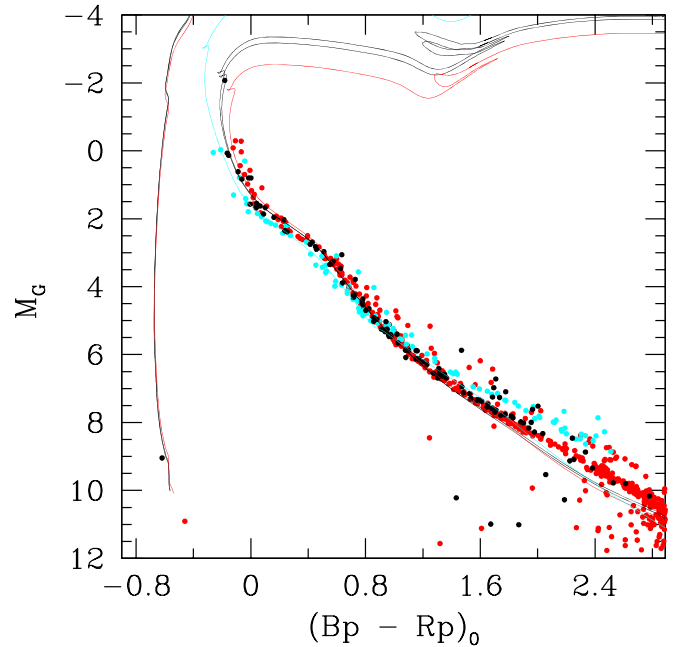
**Figure 4.** Gaia CMD of ASCC 47 (black) together with that of the Pleiades (135 Myr, red) and NGC 2451B (44 Myr, cyan) and MIST isochrones (Paxton et al. 2011, 2013, 2015; Choi et al. 2016; Dotter 2016) of the appropriate age for each cluster in the same colors. For ASCC 47, we plot two isochrones in black at 85 and 95 Myr. The age of ASCC 47 is bracketed by these two clusters from consideration of both the turnoff region of the CMD and the pre-main sequence. Our best estimate for the age of ASCC 47 is 90 ± 20 Myr.

**Table 1**
Initial–Final Mass Relation

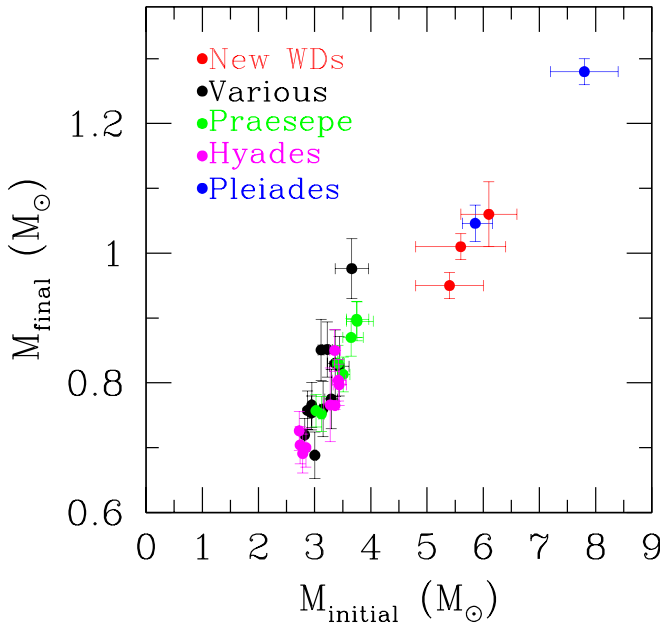| Cluster Name | Cluster Age (Myr) | WD Mass ($M_\odot$) | WD Cooling Age (Myr) | Progenitor Mass ($M_\odot$) |
|---|---|---|---|---|
| Messier 39 | 280 ± 20 | 0.95 ± 0.02 | 175 ± 25 | 5.4 ± 0.6 |
| ASCC 47 | 90 ± 20 | 1.01 ± 0.02 | 0.25 ± 0.08 | 5.6 ± 0.8 |
| Messier 47 | 150 ± 20 | 1.06 ± 0.05 | 75 ± 15 | 6.1 ± 0.5 |



**Figure 5.** Initial–final mass relation (where the initial mass is the zero-age-main-sequence mass of the progenitor and the final mass is the mass of the WD) for cluster WDs that can be found in the Gaia catalog whose progenitors had masses above 2.5 $M_\odot$. Data from Cummings et al. (2018) and Gagné et al. (2018). Error bars represent 1-$\sigma$ errors. The WDs reported in this Letter and in Paper I are in red, other colors indicate rich clusters.

mass stars to be 60% and between 23% and 90% with 95.4% confidence.

### 5. Discussion

The three WDs analyzed in this Letter are high-fidelity cluster members, and their cooling ages, when compared to the ages of their respective parent clusters, are in agreement with a single-star evolution scenario and do not require any additional delay. Furthermore, if we go back in time to the moment in which the WDs were born, the mass of the stars in the parent clusters that were evolving into WDs were too high to produce the low-mass WDs that could merge and not explode in a supernova. A merger could have still occurred, and avoided a supernova, if binary interactions on the main-sequence or the post-main-sequence phases had led to a massive progenitor engulfing a lower mass star or substellar companion. It is hard to invoke such an evolutionary scenario for all three objects though, because the binary fraction in the three clusters is very low, as can be seen from the sparsely populated binary sequences in the clusters' CMDs (Figure 3). Finding a high incidence of magnetic WDs in these young clusters therefore indicates the magnetic WDs can form directly from the evolution of single stars and do not necessarily result from the mergers of low-mass WDs.

The WDs in M 39 and in ASCC 47 do not show any indication of a companion, as their color is consistent with the temperature inferred from the spectrum. The WD in M 47 does exhibit a red excess in its spectrum that could indicate either the presence of a disk or of a colder companion (see Paper I); however, the very narrow core of the Zeeman components in the spectrum rules out the presence of a companion in a close binary. Therefore, even though we cannot exclude that the magnetic field is the result of binary interactions after the WDs were born, the fossil origin of the field is the most likely explanation for the magnetism in these newly found WDs. The birth rates of magnetic Ap/Bp stars are much lower than the average occurrence of magnetic white dwarfs (Kawka & Vennes 2004), and, therefore, magnetic main-sequence stars cannot explain the even higher incidence of magnetic WDs that we found in this range of progenitor masses.

Recent studies (Fuller et al. 2015; Cantiello et al. 2016; Stello et al. 2016) indicate that more than half of intermediate-mass stars host strong internal magnetic fields produced by powerful dynamos in their convective cores even though many do not exhibit strong surface fields like the magnetic Ap/Bp stars. In particular, they find that the presence and strength of the convectively driven magnetic dynamos in the cores show a strong dependence on stellar mass. Even more importantly, in stars with mass $M > 3\ M_\odot$, the convective core extends to a mass in the interior of the star that exceeds the mass of the WD descendant, allowing for the detection of the regions containing the high magnetic field in the final WD. This mechanism could explain why magnetic WDs are on average more massive and at the same time why we find a higher incidence of magnetic remnants from intermediate-mass stars.

**Table 2**
WD and Cluster Photometry

| Cluster | Gaia WD ID | $G_{obs}$ | $(BP - RP)_{obs}$ | $E(BP - RP)_{cluster}$ | $G_0$ | $(BP - RP)_0$ |
|---|---|---|---|---|---|---|
| Messier 47 | 3029912407273360512 | $19.796 \pm 0.006$ | $-0.134 \pm 0.106$ | $0.08 \pm 0.03$ | $11.12 \pm 0.03$ | $-0.22 \pm 0.11$ |
| Messier 39 | 2170776080281869056 | $19.193 \pm 0.003$ | $-0.179 \pm 0.050$ | $0.15 \pm 0.04$ | $11.52 \pm 0.04$ | $-0.33 \pm 0.06$ |
| ASCC 47 | 5529347562661865088 | $18.714 \pm 0.003$ | $-0.509 \pm 0.015$ | $0.11 \pm 0.04$ | $9.04 \pm 0.03$ | $-0.62 \pm 0.04$ |

**Table 3**
WD and Cluster Astrometry

| Cluster | Cluster Parallax | WD Parallax | Cluster $\mu_{R.A.}$ | Cluster $\mu_{decl.}$ | WD $\mu_{R.A.}$ | WD $\mu_{decl.}$ |
|---|---|---|---|---|---|---|
| Messier 47 | $2.072 \pm 0.096$ | $2.313 \pm 0.608$ | $-7.047 \pm 0.193$ | $0.977 \pm 0.177$ | $-7.174 \pm 0.873$ | $1.266 \pm 0.868$ |
| Messier 39 | $3.350 \pm 0.042$ | $3.309 \pm 0.277$ | $-7.472 \pm 0.131$ | $-19.848 \pm 0.152$ | $-6.631 \pm 0.462$ | $-20.181 \pm 0.456$ |
| ASCC 47 | $1.273 \pm 0.046$ | $1.299 \pm 0.214$ | $-7.839 \pm 0.355$ | $5.562 \pm 0.329$ | $-7.923 \pm 0.309$ | $5.377 \pm 0.385$ |

## Appendix A
## Cluster Membership

Stellar clusters are concentrations of stars in the phase space of position and velocity. For most stars in the catalog, Gaia gives five out of six of the phase-space coordinates: velocity across the sky (proper motion), position on the sky and distance. We identified the member stars of the two clusters by extracting all of the stars within a given radius on the sky from the center of the cluster (cone search of 2°.5 and 1°.5 for ASCC 47 and M 39, respectively). An initial photometric cut was done, discarding stars with a color excess factor above a threshold value (1.5 for ASCC 47 and 1.8 for M 39) in the Gaia parameter $B_p - R_p$. This reduced false WD candidates and contamination from non-member field stars in the final sample. Among the selected stars, we located a concentration in proper motion space and kept stars within four standard deviations of the cluster's mean proper motion. We then identified a mean parallax value for the cluster and assumed stars within four standard deviations of this central peak were members, as depicted in the left panels of Figure 1. In both clusters, we identified WDs that are indicated by red bars and crosses in Figure 1. The photometric and kinematic properties of the cluster and the WD are given in Tables 2 and 3. The reddening values that we use are the average of the Gaia reddening values of cluster members (Gaia only provides reddening values for bright stars). For a discussion on the reddening of the WDs, see Appendix C.

## Appendix B
## Spectral Fitting

The analysis of the spectroscopic data consists of several steps that we also simulate to determine our measurement uncertainties. We employ atmospheric models developed by Gianninas et al. (2010) for ASCC 47 and by Tremblay et al. (2011) for M 39. In both sets of models, the hydrogen atmosphere is computed without the assumption of local thermodynamic equilibrium; the main difference is that in the former, the composition of the atmosphere includes carbon, nitrogen, and oxygen at solar abundance ratios, while the latter are made of pure hydrogen. The addition of metals in the atmosphere is important for very hot WDs, where metal levitation in the intense radiation field can change the shape of the Balmer lines (Gianninas et al. 2010). First, we normalize the flux by fitting a tenth-order polynomial in wavelength to the spectra, avoiding the Balmer lines, to account for potential errors in the broadband calibration. We use the same

normalization procedure for both the models and the observed spectrum. We convolve the models with the instrumental Gaussian profile (5 Å). The fit is then carried out for the four Balmer lines H$\beta$, H$\gamma$, H$\delta$, and H$\epsilon$ only, using a Levenberg–Marquardt method. In the case of the non-magnetic models, our free parameters are: log$g$, $T_{eff}$, a redshift common to all lines and a zero-point shift for each line. For the magnetic case, we take the value of log$g$ to be fixed to the value determined by the photometry and allow the magnetic field to vary, together with the other parameters.

In order to understand the uncertainties in our fitting procedure, we simulate the fitting process. We take a model spectrum with the same parameters as in our best fit. To add low-frequency noise that could simulate calibration artifacts, we multiply the continuum of the spectrum with the same polynomial that we use to normalize the data. We add Gaussian noise to the resulting simulated spectrum. Finally, because our spectral data is oversampled, we smooth the simulated spectrum so that it has similar noise properties to the observations. We generate and fit an ensemble of Monte Carlo (MC) spectral observations to determine the uncertainties in our parameter fits and the significance of differences in the quality of the fits between the magnetic and non-magnetic spectral models to our data. We check that the noise properties are reproduced correctly in the simulation by making sure that the average $\chi^2$ is the same as the $\chi^2$ obtained for the best-fitting model to the real data. A sample of our simulations is shown in Figure 6: the histograms show the parameters retrieved in the MC simulation, and we find that that the distributions are Gaussian with the mean centered on the input value; the top row shows M 39 and the bottom row shows ASCC 47.

We employ simple magnetic models to fit the Balmer lines as well. As we are considering magnetic fields below 10 MG, the effect of magnetic field on the atomic structure of hydrogen reduces to the linear Zeeman effect, for which the degeneracy in the electron's energy levels in the magnetic quantum number $m_l$ is lifted, and all energy levels are shifted by an amount $\frac{1}{2}m_l h\omega_c$, where $\omega_c = eB/(m_e c)$ is the cyclotron frequency, $B$ is the magnetic field, and $m_e$ is the mass of the electron. Balmer lines are therefore split into three components, with the central component being at the same wavelength as the zero-field line and a blueshifted ($\Delta m_l = +1$) and a redshifted ($\Delta m_l = -1$) component. The separation in energy is given by $\Delta E = \pm \frac{1}{2}h\omega_c = \pm 5.79 \times 10^{-3}\left(\frac{B}{1\,MG}\right)$ eV, and therefore the shifted components are centered at the wavelengths $\lambda_0 \pm \Delta\lambda_\pm = \lambda_0\left(1 \mp \lambda_0\frac{\Delta E}{ch}\right)^{-1}$, where $\lambda_0$ is the zero-field
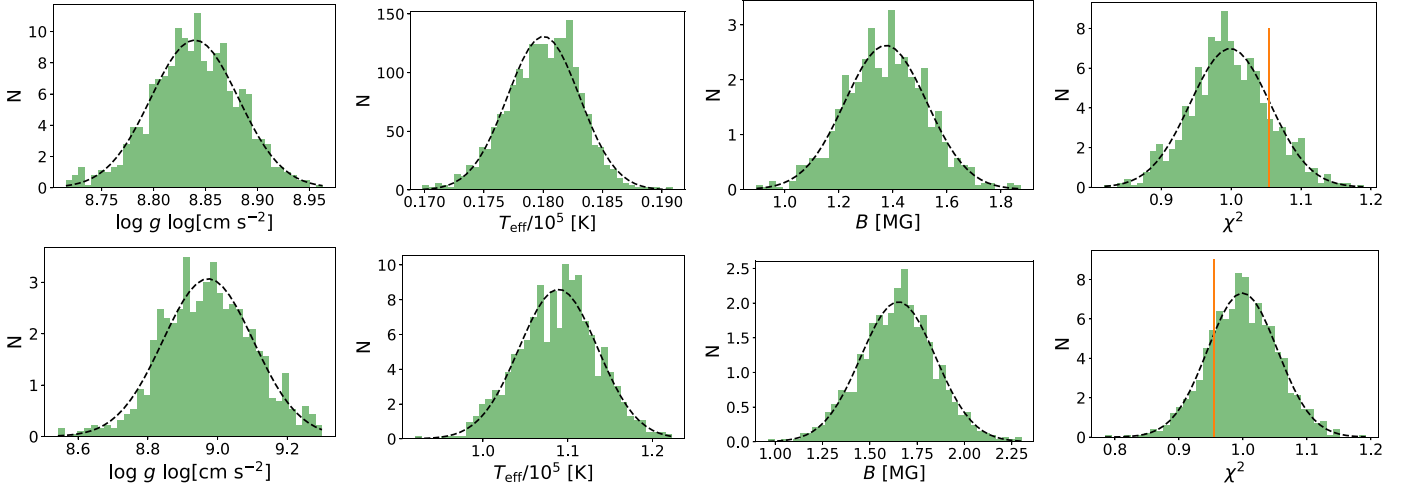
**Figure 6.** Results of our MC simulations for a total of 1000 realizations for M 39 (top row) and ASCC 47 (bottom row). The distributions for the retrieved parameters are Gaussian centered on the input parameters. The first plot in each row shows the distribution of log $g$ retrieved from the non-magnetized models; the second and the third show $T_{\rm eff}$ and $B$ retrieved from the magnetized models; the last plot shows in green the distribution of $\chi^2$ for the non-magnetic models and the orange line shows the $\chi^2$ value for the best magnetic model.

wavelength. From this linear relation between field and wavelength separation, we can infer the magnetic field strength by analyzing the splitting in the H$\alpha$ line. For both our DA WDs, the separation is about 20 Å, and therefore the field strength is about 1 MG. In this linear regime, pressure broadening is dominant, and it is safe to assume, as a first approximation, that each of the three Zeeman components are Stark broadened as in the zero-field case (Ferrario et al. 1998). Starting from the models by Gianninas et al. (2010) for ASCC 47 and the models by Tremblay et al. (2011) for M 39, we created magnetic models with the same continuum as the non-magnetic ones, and with the Balmer lines split in the three components, with each component Stark broadened as the zero-field line. The total equivalent width of each Balmer line is the same as for the zero-field case, and the central component contributes 50% of the flux, while the redshifted and blueshifted components contribute 25% each. Our models do not include any consideration on the structure of the magnetic field, as they assume the strength of the field to be the same over the surface of the stars. Using more sophisticated models, as the ones presented in Wickramasinghe & Martin (1979), Martin & Wickramasinghe (1981), and Ferrario et al. (1997), would not provide more information as the signal-to-noise and resolution in our spectra would not allow us to distinguish among possible field structures. Using the fitting procedure and simulations outlined above, we find that our best magnetic models fit the Balmer lines of the objects with a $\chi^2$ that is within one sigma of the best non-magnetic model fit, and therefore they are statistically equally good fits. The comparison is shown in the rightmost plots of Figure 6: the histogram in green shows the distribution of $\chi^2$ for the non-magnetic models and the orange line shows the $\chi^2$ value found for the best magnetic model: for ASCC 47, the best magnetic model fits the Balmer lines better than the best-fitting non-magnetic model, while for M 39 the fit is slightly worse, but both are within one sigma of the distribution.

## Appendix C
## Photometric Fitting

To estimate the masses, radii, and ages of the WDs from the photometry, we use synthetic photometric models (Bergeron et al. 2001; Holberg & Bergeron 2006; Kowalski & Saumon 2006; Tremblay et al. 2011; Blouin et al. 2018) combined with Gaia (Gaia Collaboration et al. 2018) and Pan-STARRS (Chambers et al. 2016) data for the M 39 WD and with Gaia and VPHAS+ photometry (Drew et al. 2014) for the ASCC 47 WD and the Gaia estimates of the distances to the two clusters. For both WDs we used photometry in the following bands: $G$, $B_p$, and $R_p$ from Gaia, $g$, $r$, and $i$ from Pan-STARRS and VPHAS+. The photometry was insufficient to determine the interstellar reddening to the white dwarf, so we marginalized our fitting procedure over the measured reddening values for the stars in each cluster from Gaia and applied reddening corrections (Cardelli et al. 1989; O'Donnell 1994) to our synthetic photometry models. Figure 7 depicts the one through 5-$\sigma$ confidence regions for the fits to the photometric data. The width of the confidence region is mainly determined by the uncertainty in the distances to the clusters. The vertical span of the confidence region results from the uncertainty in the interstellar absorption toward the WDs. On both plots, the temperature and surface gravity determined by fitting non-magnetic spectral models to the spectroscopic data are depicted with red error bars. For neither WD is the photometry consistent with the surface gravity and temperature measured in this way. Because of the uncertainty in the interstellar reddening, the photometry cannot constrain the temperature on its own. However, the strength of the spectral lines depends strongly on the temperature of the star (and is independent of the reddening), so we can use the spectroscopy to constrain the temperature and find a value of the surface gravity and temperature that is consistent with the photometry and spectroscopy as long as the white dwarf has a magnetic field on the order of a million Gauss (the difference in temperature between fitting a magnetic or a non-magnetic model is small, within the error bars; see the main text). The photometric fitting also yields an estimate of the ages of the two WDs: 250 ± 80 kyr for ASCC 47 and 175 ± 25 Myr for M 39.
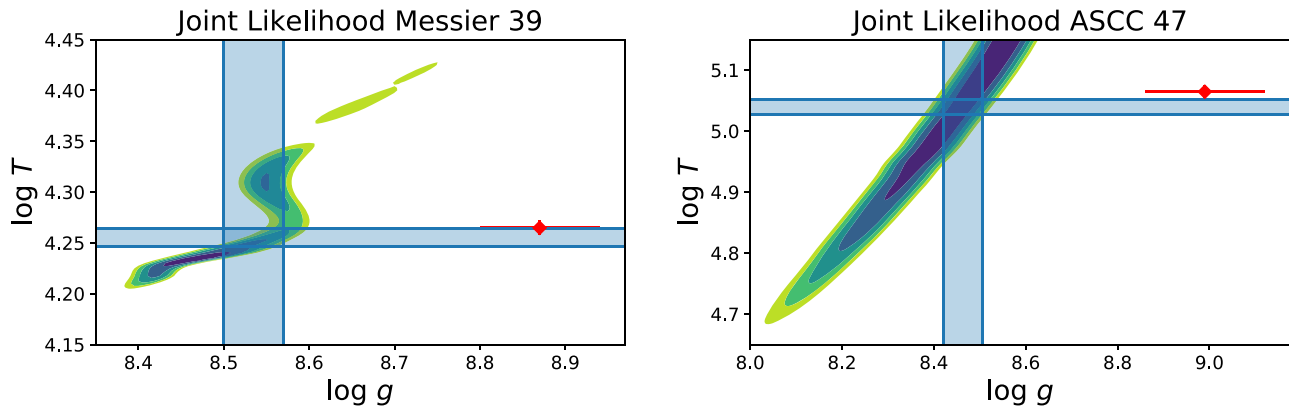
**Figure 7.** Joint likelihoods for the fits of the photometric data for the WDs in Messier 39 and ASCC 47 to white-dwarf models. The values of the surface gravity and temperature obtained from the spectroscopic fits using non-magnetic models are depicted with red error bars. The corresponding best-fit temperature range from spectroscopic fits with magnetic models are shown with a horizontal band. These constraints combined with the photometric fits yield a confidence interval on the surface gravity depicted by the vertical band.

When we combine these estimates for the ages of the WDs with the cluster ages, we can estimate the initial masses of the stars that became the two WDs as tabulated in Table 1 in the main text.

## Appendix D
## Gaia Cluster White Dwarfs

We are interested in the total number of cluster white dwarfs with progenitor masses above 5 $M_\odot$ whose cluster membership can be confirmed through Gaia astrometry. In order to select the sample of cluster white dwarfs that is shown in Figure 5 in the main text, we selected all the white dwarfs known to be cluster members that are also part of the Gaia catalog and checked their membership using Gaia astrometry. Some known WDs that are likely associated with clusters are too faint to be in Gaia and therefore we did not include them. In the progenitor mass range above 5 $M_\odot$, we found four white dwarfs in Gaia that were previously associated with clusters. We retained two of them, GD 50 and EGGR 25. EGGR 25 respects our standards for cluster membership in the Pleiades, while GD 50, the most massive object in our sample, is located well outside of the Pleiades cluster boundary. A recent study showed that GD 50 is very likely a member of the AB Doradus moving group (Gagné et al. 2018), which is virtually coeval with the Pleiades, and therefore we can still include the white dwarf in our sample as we can infer a progenitor mass. The remaining two are a white dwarf in NGC 1039 (WD 17; Rubin et al. 2008) and PG 0136+251, historically associated with the Pleiades (Dobbie et al. 2006). Both the parallax and proper motion of the first object rule out its membership in NGC 1039, and we therefore excluded this WD from our sample. We performed a similar analysis as in Gagné et al. (2018) for PG 0136+251 and we ruled out its membership in both the Pleiades cluster and the moving group AB Doradus. Although PG 0136+251, the Pleiades and AB Doradus share approximately the same common motion, we find that PG 0136+251 was actually further from the Pleiades and from AB Doradus in the past (independently of its line-of-sight velocity), so we excluded this WD from our sample as well.

## ORCID iDs

Ilaria Caiazzo ⓘ https://orcid.org/0000-0002-4770-5388
Jeremy Heyl ⓘ https://orcid.org/0000-0001-9739-367X
Harvey Richer ⓘ https://orcid.org/0000-0001-9002-8178
Jeffrey Cummings ⓘ https://orcid.org/0000-0001-7453-9947
Leesa Fleury ⓘ https://orcid.org/0000-0002-7022-8380
James Hegarty ⓘ https://orcid.org/0000-0003-0933-945X
Pier-Emmanuel Tremblay ⓘ https://orcid.org/0000-0001-9873-0121

## References

Bergeron, P., Leggett, S. K., & Ruiz, M. T. 2001, ApJS, 133, 413
Blouin, S., Dufour, P., & Allard, N. F. 2018, ApJ, 863, 184
Bressan, A., Marigo, P., Girardi, L., et al. 2012, MNRAS, 427, 127
Cantiello, M., Fuller, J., & Bildsten, L. 2016, ApJ, 824, 14
Cardelli, J. A., Clayton, G. C., & Mathis, J. S. 1989, ApJ, 345, 245
Chambers, K. C., Magnier, E. A., Metcalfe, N., et al. 2016, arXiv:1612.05560
Choi, J., Dotter, A., Conroy, C., et al. 2016, ApJ, 823, 102
Cummings, J. D., & Kalirai, J. S. 2018, AJ, 156, 165
Cummings, J. D., Kalirai, J. S., Tremblay, P. E., Ramirez-Ruiz, E., & Choi, J. 2018, ApJ, 866, 21
Dobbie, P. D., Napiwotzki, R., Lodieu, N., et al. 2006, MNRAS Letters, 373, L45
Dotter, A. 2016, ApJS, 222, 8
Drew, J. E., Gonzalez-Solares, E., Greimel, R., et al. 2014, MNRAS, 440, 2036
Ferrario, L., Vennes, S., & Wickramasinghe, D. T. 1998, MNRAS, 299, L1
Ferrario, L., Wickramasinghe, D. T., & Kawka, A. 2020, arXiv:2001.10147
Ferrario, L., Vennes, S., Wickramasinghe, D. T., Bailey, J. A., & Christian, D. J. 1997, MNRAS, 292, 205
Fuller, J., Cantiello, M., Stello, D., Garcia, R. A., & Bildsten, L. 2015, Sci, 350, 423
Gagné, J., Fontaine, G., Simon, A., & Faherty, J. K. 2018, ApJL, 861, L13
Gaia Collaboration, Prusti, T., de Bruijne, J. H. J., et al. 2016, A&A, 595, A1
Gaia Collaboration, Brown, A. G. A., Vallenari, A., et al. 2018, A&A, 616, A1
García-Berro, E., Lorén-Aguilar, P., Aznar-Siguán, G., et al. 2012, ApJ, 749, 25
Gentile Fusillo, N. P., Nicola, P., Tremblay, P.-E., et al. 2019, MNRAS, 482, 4570
Gianninas, A., Bergeron, P., Dupuis, J., & Ruiz, M. T. 2010, ApJ, 720, 581
Gianninas, A., Bergeron, P., & Ruiz, M. T. 2011, ApJ, 743, 138
Holberg, J. B., & Bergeron, P. 2006, AJ, 132, 1221
Hollands, M. A., Tremblay, P. E., Gänsicke, B. T., Gentile-Fusillo, N. P., & Toonen, S. 2018, MNRAS, 480, 3942
Kawka, A., & Vennes, S. 2004, in IAU Symp. 224, The A-Star Puzzle, ed. J. Zverko et al. (Cambridge: Cambridge Univ. Press), 879
Kawka, A. 2020, arXiv:2001.10672
Kawka, A., Vennes, S., Schmidt, G. D., Wickramasinghe, D. T., & Koch, R. 2007, ApJ, 654, 499
Kowalski, P. M., & Saumon, D. 2006, ApJL, 651, L137
Landstreet, J. D., & Bagnulo, S. 2019, A&A, 628, A1
Martin, B., & Wickramasinghe, D. T. 1981, MNRAS, 196, 23
McCleery, J., Tremblay, P.-E., Gentile Fusillo, N. P., et al. 2020, arXiv:2006.00874
Moss, D. 2003, A&A, 403, 693

Nomoto, K. 1987, ApJ, 322, 206

Nordhaus, J., Wellons, S., Spiegel, D. S., Metzger, B. D., & Blackman, E. G. 2011, PNAS, 108, 3135

O'Donnell, J. E. 1994, ApJ, 422, 158

Paxton, B., Bildsten, L., Dotter, A., et al. 2011, ApJS, 192, 3

Paxton, B., Cantiello, M., Arras, P., et al. 2013, ApJS, 208, 4

Paxton, B., Marchant, P., Schwab, J., et al. 2015, ApJS, 220, 15

Richer, H. B., Kerr, R., Heyl, J., et al. 2019, ApJ, 880, 75

Rubin, K. H. R., Williams, K. A., Bolte, M., & Koester, D. 2008, AJ, 135, 2163

Shen, K. J. 2015, ApJL, 805, L6

Stello, D., Cantiello, M., Fuller, J., et al. 2016, Natur, 529, 364

Tody, D. 1986, Proc. SPIE, 627, 733

Tout, C. A., Wickramasinghe, D. T., & Ferrario, L. 2004, MNRAS, 355, L13

Tout, C. A., Wickramasinghe, D. T., Liebert, J., Ferrario, L., & Pringle, J. E. 2008, MNRAS, 387, 897

Tremblay, P. E., Bergeron, P., & Gianninas, A. 2011, ApJ, 730, 128

Wickramasinghe, D. T., & Martin, B. 1979, MNRAS, 188, 165

Wickramasinghe, D. T., Tout, C. A., & Ferrario, L. 2014, MNRAS, 437, 675

Woltjer, L. 1964, ApJ, 140, 1309